DOI: 10.1478/AAPP.1002A11

AAPP | Atti della Accademia Peloritana dei Pericolanti
Classe di Scienze Fisiche, Matematiche e Naturali
ISSN 1825-1242

Vol. 100, No. 2, A11 (2022)

NATURAL RADIOACTIVITY CONTENT AND MINERALOGICAL COMPOSITION OF BEACH SANDS FROM THE GULF OF SQUILLACE, SOUTHERN ITALY: A CASE STUDY

FRANCESCO CARIDI [a], SEBASTIANO ETTORE SPOTO [a], GIUSEPPE PALADINI [a], VALENTINA VENUTI [a], VINCENZA CRUPI [a], MICHELA RICCA [b] AND DOMENICO MAJOLINO [a*]

ABSTRACT. This article reports a case study on the natural radioactivity content of beach sands from the Gulf of Squillace, Ionian coast of Calabria, Southern Italy, including the assessment of the natural activity concentration and the resulting estimation of the radiological health risk, related to their mineralogical phase composition. The analysis of the natural radioisotopes content was performed by using High Purity Germanium (HPGe) gamma-ray spectrometry, with the aim of quantifying the mean activity concentration of ^{226}Ra, ^{232}Th, and ^{40}K. Radiological hazard indices were thus estimated, in order to evaluate any possible radiological risk for the population that uses to spend summer holidays on this renowned tourist destination. Moreover, the identification of the source of the aforementioned naturally occurring radionuclides was attempted by X-Ray Fluorescence (XRF) spectroscopy and Micro-Raman Scattering (MRS), thereby recognizing the main radioisotope-bearing minerals present in the studied beach sands. The obtained results can also be used as a baseline for future investigations regarding background radioactivity levels of the studied area.

1. Introduction

Natural radioactivity, mainly due to the presence of primordial radionuclides in the Earth's crust (Rosell *et al.* 1991; Ghrefat and Yusuf 2006), provides the greatest contribution to the ionizing radiations dose received by the human beings (Papadopoulos *et al.* 2014; Paiva *et al.* 2015). In particular, radioisotopes belonging to ^{238}U, ^{232}Th, ^{235}U radioactive chains, together with the primordial ^{40}K (Ravisankar *et al.* 2012), are commonly found, together with their products of decay (Caridi *et al.* 2016a, 2017a), in environmental matrices, such as water, rocks and soils. Moreover, natural radioactivity widely varies according to the geomorphological, mineralogical and geographical features of the investigated site (Caridi *et al.* 2017c). Beach sands, in particular, are the result of erosion and weathering of metamorphic and igneous rocks, characterized by the highest levels of natural radionuclides (Caridi *et al.* 2016b,c). Thus, an investigation focused on the evaluation of the activity concentration of natural radioisotopes in beach sands allows to evaluate the radiological risk due to the external gamma radiation exposure for individuals who spend their holidays

on these beaches. Moreover, geochemical studies of these soils can be helpful in order to understand the elements distribution patterns and to evaluate the environmental conditions existing in a specific area, as well as to trace the provenance of the main radioisotope-bearing minerals, according to the information of the surrounding geological setting (Caridi *et al.* 2021b; Shahrokhi and Kovacs 2021). In addition, the assessment of their mineralogical-compositional properties can provide information regarding the geological history of the transport and sorting process (Caridi *et al.* 2016d; Sabatino *et al.* 2019).

In this article, a multi-technique approach, including the use of several analytical methods such as High Purity Germanium (HPGe) gamma-ray spectrometry, X-Ray Fluorescence (XRF) spectroscopy and Micro-Raman Scattering (MRS), was employed on a variety of beach sands, coming from three different sites in the area of the Gulf of Squillace, Ionian coast of Calabria[1], Southern Italy. The study was aimed at finding a correlation between the natural radioactivity content and the mineralogical-geochemical composition of the investigated area, that constitutes a popular touristic destination, especially in summer. In this regard, calculations of radiological health risk indices were also performed, to assess any possible radiological hazard for tourists or the inhabitant population.

2. Materials and methods

2.1. Geological notes and sampling. The geological map of the Gulf of Squillace is shown in Fig. 1, with the sampling sites, labelled as ID# (# = 1, 2, 3) indicated. Their GPS coordinates are reported in Table 1, together with the number of sand samples taken from each site. The area under study belongs to the Calabrian Arc segment, extending to

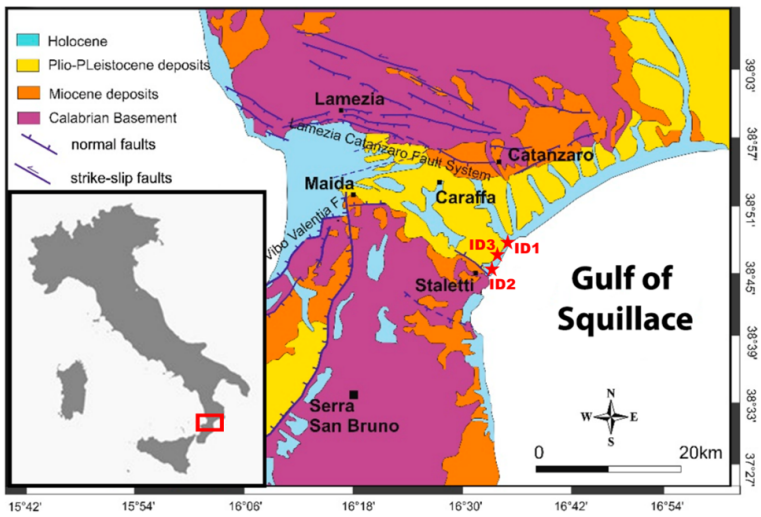

FIGURE 1. The geological map of the Gulf of Squillace (modified from Pirrotta *et al.* 2021), with the sampling sites, labelled as ID# (# = 1, 2, 3) indicated.

[1]https://www.regione.calabria.it/website/organizzazione/dipartimento10/

TABLE 1. The GPS coordinates of the sampling sites, together with the number of sand samples taken from each one.

Sampling site			
ID	**Latitude**	**Longitude**	**Number of samples**
1	38° 43' 19" N	16° 32' 20" E	5
2	38° 45' 51" N	16° 34' 03" E	5
3	38° 46' 38" N	16° 34' 33" E	5

the Southern portion of the Coastal Chain (Fiannacca *et al.* 2015; Vitale *et al.* 2019) and consisting in a series of Palaeozoic plutonic-metamorphic nappes, locally overlain by a Mesozoic-Cenozoic sedimentary cover (Calcaterra and Parise 2010). The area is mainly composed by heterogeneous crystalline-metamorphic rocks and their related weathering products and is characterized by two distinct time- and, partly, space-related granitoid associations: (i) a calc-alkaline suite, compositionally expanded (SiO_2 = 48-70%) and biotite-dominated, which represents the 70% of the exposed plutonites and (ii) a strongly peraluminous suite, compositionally restricted (SiO_2 = 67-76%) and containing two-micas and Al-silicates (Rottura *et al.* 1990). The peraluminous typologies contain xenoliths of migmatitic metapelites and abundant large crystals of almandine-rich garnet. Garnets typically exhibit multiple corona-like rims, suggestive of a protracted melt-rock interaction (Rottura *et al.* 1990).

2.2. HPGe gamma spectrometry analysis. For the gamma spectrometry measurements, the samples, collected at a depth of 0-15 cm, were dried at 105 °C in an oven, sieved to obtain a particle size less than 2 mm, then inserted in Marinelli hermetically sealed containers of 1 L capacity and left for a period of 40 days in order to reach the secular radioactive equilibrium between ^{226}Ra and its daughter products. After that, the specific activity of ^{226}Ra was quantified. An acquisition time of 70000 s was used. The 295.21 and 351.92 keV ^{214}Pb and 1120.29 keV ^{214}Bi gamma-ray lines were used to quantify the ^{226}Ra specific activity. The ^{232}Th activity concentration was determined by using the 911.21 and 968.97 keV ^{228}Ac gamma-ray lines; it can be assumed that ^{228}Ra, ^{228}Ac and ^{228}Th were in secular equilibrium with the parent nuclide ^{232}Th (Caridi *et al.* 2017b). Regarding ^{40}K, the evaluation was performed from its γ-line at 1460.8 keV.

The experimental set-up was composed by a positive biased Ortec HPGe detector (GMX), whose operating parameters are reported in Table 2. It was placed inside lead wells to shield the background radiation environment. Efficiency and energy calibrations were performed using a multipeak Marinelli geometry gamma source (AK 5901) of 1 L capacity, covering the 59.54 keV-1836 keV energy range, customized to reproduce the exact geometries of samples in a water-equivalent epoxy resin matrix. The Gamma Vision (Ortec) software was used for data acquisition and analysis (Caridi *et al.* 2019a). The activity concentration (Bq kg^{-1}) of the investigated radionuclide was calculated using the following formula (Caridi *et al.* 2021a):

$$C = \frac{N_E}{\varepsilon_E t \gamma_d V} \tag{1}$$

TABLE 2. The Ortec HPGe detector (GMX) operating parameters.

HPGe GMX detector	
Parameter	**Value**
Full Width at Half Maximum	1.94 keV
Peak to Compton ratio	65:1
Relative efficiency	37.5% (at the 1.33 MeV ^{60}Co γ-line)
Bias voltage	- 4800 V
Energy range	5 keV – 2 MeV

where N_E indicates the net area of the radioisotope photopeak, ε_E and γ_d are the efficiency and yield of the photopeak, respectively, V is the volume of the sample (L) and t the live time (s).

2.3. Radiological hazard indices assessment.

2.3.1. *Radium equivalent activity.* In order to represent the ^{226}Ra, ^{232}Th and ^{40}K activity concentrations by a single quantity, which takes into account the radiation hazards associated with them, a radiological index called Radium equivalent activity (Ra_{eq}) was introduced, used to ensure the uniformity of the distribution of natural radionuclides ^{226}Ra, ^{232}Th and ^{40}K and given by (Beretka and Matthew 1985):

$$Ra_{\mathrm{eq}}(Bq\ kg^{-1}) = C_{\mathrm{Ra}} + 1.43C_{\mathrm{Th}} + 0.077C_{\mathrm{K}} \tag{2}$$

where C_{Ra}, C_{Th} and C_{K} are the specific activities of ^{226}Ra, ^{232}Th, and ^{40}K, respectively. In the above formula, the numerical coefficients are evaluated assuming that 370 Bq kg^{-1} of ^{226}Ra, 259 Bq kg^{-1} of ^{232}Th and 4810 Bq kg^{-1} of ^{40}K produce the same gamma-ray dose rate. The maximum Ra_{eq} must be less than 370 Bq kg^{-1} to exclude radiological hazard effects for the local population (Ramasamy *et al.* 2011).

2.3.2. *Excess lifetime cancer risk (ELCR).* The excess lifetime cancer risk (*ELCR*) index expresses the probability of developing cancer over a lifetime at a given exposure level. It represents the number of extra cancers expected in a given population as a consequence of the exposure to a carcinogen at a given dose, and is given by (Avwiri and Egieya 2013):

$$ELCR = AEDE \times D_L \times R_F \tag{3}$$

where *AEDE* is the annual effective dose equivalent, D_L the average duration of life (estimated to be 70 years) and R_F the risk factor (Sv^{-1}), *i.e.*, fatal cancer risk per Sievert (Taskin *et al.* 2009). For stochastic effects, International Commission on Radiological Protection (ICRP) recommends, for this last parameter, a value of 0.05 for the public (Taskin *et al.* 2009).

2.4. X-Ray Fluorescence. XRF measurements were carried out using a portable XRF Alpha 4000 (Innov-X systems, Inc., Woburn, MA, USA) analyzer, which allows the detection of chemical elements with an atomic number (Z) between phosphorus and lead. It is equipped with a Ta anode X-Ray tube as source and a Si PIN diode (active area $\sim$170 mm^2) as detector. For each point, two sequential tests were performed, the first one with operating

conditions of 40 kV and 7 μA, and the second one with 15 kV and 5 μA, for a total spectrum collection time of 120 s. The instrument was controlled by a Hewlett-Packard iPAQ Pocket PC, which was also used for the data storage. The calibration was performed using a soil light element analysis program (LEAP) II and was verified using alloy certified reference materials produced by Analytical Reference Materials International. When detected, peaks at ~8.15 keV and ~9.34 keV have to be ascribed to L_α and L_β transitions of Ta anode. When Cu is present, the L_α line of Ta is superimposed to the K_α line of Cu.

2.5. Micro-Raman Scattering. Micro-Raman Scattering (MRS) measurements were performed by using a portable "BTR 111 Mini-RamTM" (B&W Tek, Inc., Newark, NJ, USA) spectrometer with an excitation wavelength of 785 nm (diode laser), a maximum laser power of 280 mW at the excitation port, and a charge coupled device (CCD) detector (thermoelectric cooled, TE). It was possible to continuously adjust the laser output power in order to obtain the best signal-to-noise ratio in the minimum integration time. The 62-3153 cm^{-1} spectral range was investigated, with a resolution of 10 cm^{-1}, and an acquisition time of 10 s $\times$ 32 scans. The optimal performance of the instrument was guaranteed by a calibration procedure before each measurement using the peak at 520.6 cm^{-1} of a silicon chip. The system was equipped with a BAC151B Raman microscope. An 80$\times$/40$\times$ objective was used, with a working distance of 1.25 mm/3.98 mm and laser beam spot size 26 μm/50 μm. The maximum power at the samples was ~15 mW. Punctual analyses were performed on small samples quantities (about 2 mg). Due to the micrometric size of the grains, a microscopic approach was mandatory in order to select by visual inspection the grains of suspected interest and to that guarantee a good S/N ratio. For each sample, we collected 15-20 spectra from different grains.

For a reliable assignment of the bands, spectra were compared with literature (Caridi *et al.* 2019b). The abbreviations of minerals reported in the present study follow the list approved by the International Mineralogical Association (IMA) Commission on New Minerals, Nomenclature and Classification (CNMNC) (Warr 2021).

3. Results and discussion

3.1. Radioactivity analysis. For all the investigated samples, the mean activity concentration of ^{226}Ra, ^{232}Th, and ^{40}K, calculated according to Eq. 1, is reported in Table 3. Worldwide average specific activity of ^{226}Ra, ^{232}Th and ^{40}K are 35, 30 and 400 Bq kg^{-1},

TABLE 3. The mean activity concentration of ^{226}Ra, ^{232}Th, and ^{40}K for all the investigated samples.

	Activity concentration (Bq kg^{-1})		
Site ID	**^{226}Ra**	**^{232}Th**	**^{40}K**
1	7.7 $\pm$0.7	25.8 $\pm$ 3.1	751 $\pm$ 95
2	15.1 $\pm$ 1.3	275 $\pm$ 34	498 $\pm$ 95
3	59.9 $\pm$ 6.1	521 $\pm$ 69	152 $\pm$ 22

respectively (UNSCEAR 2000). In the light of this, experimental results here reported show that, in our samples, the specific activity of ^{226}Ra is higher than the average worldwide value only for ID3 site; for ^{232}Th, it is higher than the worldwide one for ID2 and ID3 sites. The activity concentration of ^{40}K is higher than the average worldwide value for ID1 and ID2 sites. These anomalous behaviours deserve a more critical interpretation, that will be given in the following in terms of the mineralogical composition of the beach sands themselves.

3.2. Radiological hazard effects assessment. Table 4 reports the radiological hazard indices, Ra_{eq} and *ELCR*, evaluated according to Eqs. 2 and 3, respectively. In particular, the

TABLE 4. The radiological hazard indices, Ra_{eq} and *ELCR*.

Site ID	Ra_{eq} (Bq kg^{-1})	*ELCR* ($\times 10^{-3}$)
1	50	0.05
2	194	0.21
3	349	0.37

Ra_{eq} turned out to be equal to 50 Bq kg^{-1}, 194 Bq kg^{-1}, and 349 Bq kg^{-1} for ID1, ID2 and ID3 sites, respectively. All values are lower than the maximum recommended one of 370 Bq kg^{-1}, thus reasonably excluding hazard effects for the population, from the radiological point of view. The *ELCR* values, obtained by using in Eq. 3 *AEDE* values reported in literature for similar investigations in the studied area (Caridi *et al.* 2021c), are 0.05×10^{-3}, 0.21×10^{-3} and 0.37×10^{-3} for ID1, ID2 and ID3 sites, respectively. Worth of note, a linear relationship between *ELCR* and the annual effective dose equivalent is found, as shown in Fig. 2, in good agreement with the literature (Qureshi *et al.* 2014). It is important

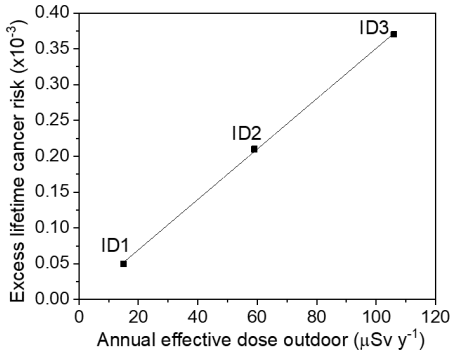

FIGURE 2. The linear relationship between *ELCR* and the annual effective dose equivalent.

to underline that the evaluation of the radiological health hazards for the population, only on the basis of the calculated excess lifetime cancer risk, is not possible, since reliable and standardized mortality and morbidity statistics are not accessible.

3.3. Mineralogical composition. Figure 3a reports the XRF spectrum collected on a representative sample coming from ID1 site, showing the presence of K along with Fe, Ca, Ti, and Mn as major elements. Figure 3(b-c) shows the Raman spectra collected on different grains of the same sample. For several grains, α-quartz (SiO_2) was detected (Fig. 3b), as

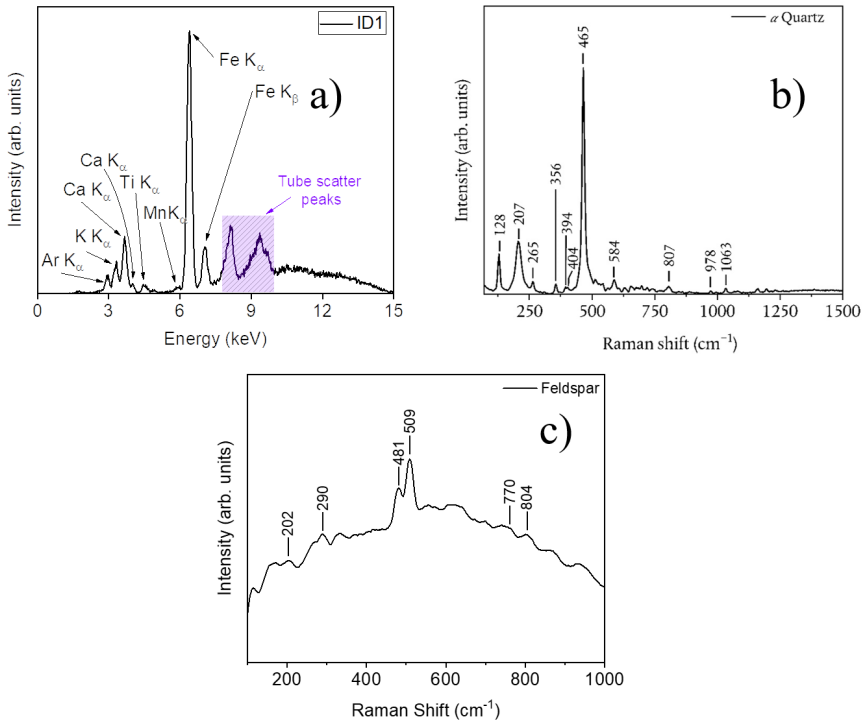

FIGURE 3. The XRF spectrum collected on a representative sample coming from ID1 site (a). The α-quartz Raman spectrum, being the average of 7 measurements exhibiting similar profiles (b), and the feldspar Raman spectrum, being the average of 10 measurements exhibiting similar profiles (c), collected on different grains of the same sample.

identified by the well-known characteristic Raman active modes (Krishnamurti 1958). In other areas, feldspars (Fig. 3c) are revealed, as recognized according to (Chopelas 1999; Freeman *et al.* 2008). In the spectrum, the two strongest Raman peaks in the 450-520 cm^{-1} region are ascribed to the ring-breathing modes of the four-membered rings of tetrahedra (Mckeown 2005). A comparison with literature (Freeman *et al.* 2008) put in evidence that the investigated feldspars are present as a solid solution of a K-feldspar (orthoclase and/or microcline), as main component, and minor components of albite ($NaAlSi_3O_8$) and anorthite ($CaAl_2Si_2O_8$). The obtained result is supported by the detection of potassium from XRF data, and allows us to hypothesize K-feldspar ($KAlSi_3O_8$) as the main radioisotope-bearing mineral present in the analyzed beach sands, thus explaining the highest specific activity of the radionuclide ^{40}K in this site with respect to the surrounding area (see Table 3).

As far as samples from ID2 site are concerned, XRF results, as evidenced in a representative spectrum reported in Fig. 4a, show an elemental qualitative composition quite similar to that of samples from ID1 site. MRS analysis revealed a first group of grains characterized by an abundance of α-quartz (spectrum not reported), a second group composed by feldspars (spectrum not reported), and a third group whose average spectrum is reported in Fig. 4b. In

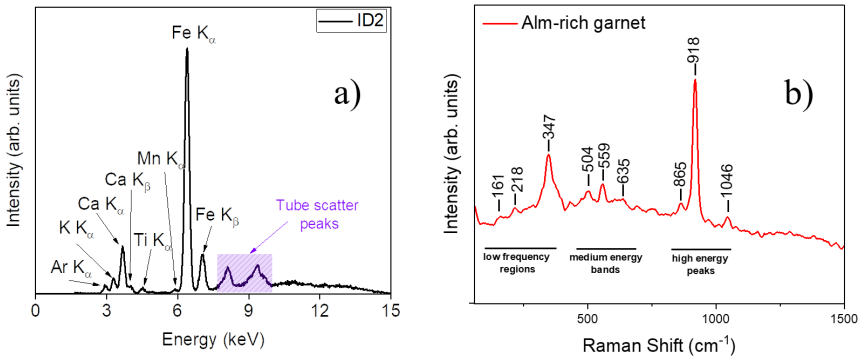

FIGURE 4. The XRF spectrum collected on a representative sample coming from ID2 site (a). The almandine-rich garnet Raman spectrum, being the average of 7 measurements exhibiting similar profiles, collected on different grains of the same sample (b).

the spectrum, the two Raman bands at ~161 cm^{-1} and ~218 cm^{-1} are respectively assigned to Fe^{2+} (Kos *et al.* 2020) and SiO_4 (Kolesov and Geiger 1998) translation motions, the band at ~347 cm^{-1} comes from rotation motions of SiO_4 ("RUFF Library" 2021), the three bands at ~504 cm^{-1}, ~559 cm^{-1} and ~635 cm^{-1}, are ascribed to Si–O bending modes, and, finally, the three peaks in the 850-1100 cm^{-1} range are assigned to Si–O stretching, either symmetric or asymmetric (Kos *et al.* 2020). From a comparison with literature (Mingsheng *et al.* 1994; Kos *et al.* 2020), almandine-rich garnets ($Fe^{2+}{}_3Al_2Si_3O_{12}$) were recognized. Also in this case, the presence of K-feldspars and almandine-rich garnets, as revealed by MRS, other than resulting in a good agreement with the observation, by XRF, of K, Ti and Fe as major elements, can explain the measured high activity concentration of ^{40}K and ^{232}Th in ID2 site (see Table 3).

Finally, regarding samples from ID3 site, the XRF results (Fig. 5a) evidenced an elemental composition mainly Fe- and Ti-based. MRS data gave evidence of grains rich in α-quartz (spectrum not reported), almandine-rich garnet (spectrum not reported), and ilmenite ($Fe^{2+}TiO_3$) (Fig. 5b), characterized according to (Wang *et al.* 2004; Smyth *et al.* 2014; Vennari and Williams 2021). Based on these papers, the highest Raman peak in the spectrum, centered at ~680 cm^{-1}, can be attributed to the A_g mode, *i.e.*, the symmetric stretching vibration of $Ti^{4+}O_6$ octahedra, it is accompanied by a shoulder at ~610 cm^{-1}, representing octahedral breathing motions of E_g symmetry. Going on, the peak at ~162 cm^{-1} describes the A_g mode associated with translations of Fe^{2+} against the oxygen framework, the peak at ~232 cm^{-1} arises from A_g mode predominantly due to translations of the $Ti^{4+}O_6$ octahedra against the Fe^{2+} ions. The features observed at ~331 cm^{-1}, ~369

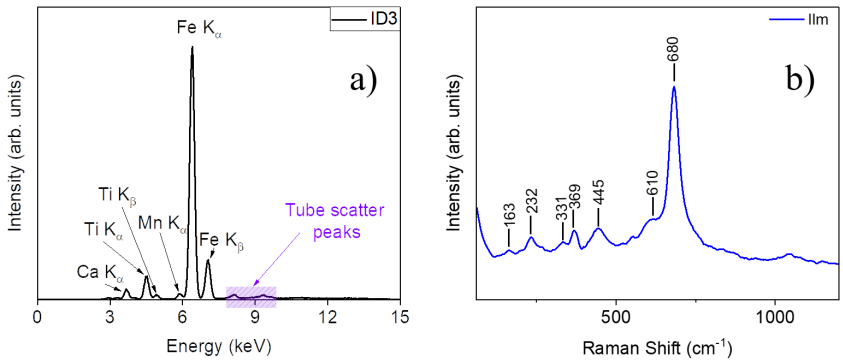

FIGURE 5. The XRF spectrum collected on a representative sample coming from ID3 site (a). The ilmenite Raman spectrum, being the average of 8 measurements exhibiting similar profiles, collected on different grains of the same sample (b).

cm^{-1} and ~443 cm^{-1} are associated with O-Ti-O bends, of E_g (the first one) and A_g (the last two) symmetry, respectively. Worth of note, the simultaneous presence, in samples from ID3 site, of ilmenites and almandine-rich garnets, also in this case in accordance with the elemental analysis carried out by XRF, can furnish a reasonable explanation for the high abundance of ^{226}Ra and ^{232}Th detected in this site (see Table 3).

4. Conclusions

The natural radioactivity of beach sands from the Gulf of Squillace, Ionian coast of Calabria, Southern Italy, was investigated through High Purity Germanium (HPGe) gamma-ray spectrometry. Calculations of the radium equivalent activity (Ra_{eq}) and of the excess lifetime cancer risk (*ELCR*) were performed to assess any possible radiological hazard for the population that spends holidays on this popular tourist destination, especially in summer. In particular, values of Ra_{eq} were found to be lower than the maximum recommended one for the population members, thus reasonably excluding radiological hazard effects.

In addition, X-Ray Fluorescence (XRF) and Micro-Raman Scattering (MRS) techniques were applied in order to correlate the radioactivity emission to the mineralogical/geochemical composition of the investigated sands. From the results, we can conclude that: (i) in the case of ID1 site, the anomalous high value of the ^{40}K specific activity can be mainly due to the abundant presence of K-feldspar in the beach sands; (ii) as far as ID2 site is concerned, the anomalous high value of the ^{40}K and ^{232}Th specific activity can be explained taking into account, in the mineralogical composition of samples from this site, the abundant presence of K-feldspar and almandine-rich garnets respectively; (iii) in ID3 site, the anomalous high values of ^{226}Ra and ^{232}Th specific activity can be mainly due to ilmenites and almandine-rich garnets, respectively, as significant mineralogical phases of the investigated samples.

References

Avwiri, G. O. and Egieya, J. M. (2013). "Radiometric assay of hazard indices and excess lifetime cancer risk due to natural radioactivity in soil profile in Ogba/Egbema/Ndoni local government area of Rivers state, Nigeria". *Academic Research International* **4**(5), 54–65. URL: https://www.semanticscholar.org/paper/RADIOMETRIC-ASSAY-OF-HAZARD-INDICES-AND-EXCESS-RISK-Avwiri-Egieya/eb459c41e67b00cffffbffb86875bd96a5ba6876.

Beretka, J. and Matthew, P. J. (1985). "Natural radioactivity of Australian building materials, industrial wastes and by-products". *Health physics* **48**(1), 87–95. DOI: 10.1097/00004032-198501000-00007.

Calcaterra, D. and Parise, M. (2010). "Weathering in the crystalline rocks of Calabria, Italy, and relationships to landslides". In: *Weathering as a Predisposing Factor to Slope Movements*. Geological Society, London, Engineering Geology Special Publications, pp. 105–130. DOI: 10.1144/EGSP23.7.

Caridi, F., D'Agostino, M., Belvedere, A., Marguccio, S., and Belmusto, G. (2016a). "Radon radioactivity in groundwater from the Calabria region, south of Italy". *Journal of Instrumentation* **11**(05), P05012. DOI: 10.1088/1748-0221/11/05/P05012.

Caridi, F., D'Agostino, M., Belvedere, A., Marguccio, S., Belmusto, G., and Gatto, M. (2016b). "Diagnostics techniques and dosimetric evaluations for environmental radioactivity investigations". *Journal of Instrumentation* **11**, C10012. DOI: 10.1088/1748-0221/11/10/C10012.

Caridi, F., D'Agostino, M., Messina, M., Marcianò, G., Grioli, L., Belvedere, A., Marguccio, S., and Belmusto, G. (2017a). "Lichens as environmental risk detectors". *European Physical Journal Plus* **132**(4), 189. DOI: 10.1140/epjp/i2017-11459-y.

Caridi, F., Marguccio, S., Belvedere, A., Belmusto, G., Marcianò, G., Sabatino, G., and Mottese, A. (2016c). "Natural radioactivity and elemental composition of beach sands in the Calabria region, south of Italy". *Environmental Earth Sciences* **75**(7), 629. DOI: 10.1007/s12665-016-5393-z.

Caridi, F., Marguccio, S., D'Agostino, M., Belvedere, A., and Belmusto, G. (2016d). "Natural radioactivity and metal contamination of river sediments in the Calabria region, south of Italy". *European Physical Journal Plus* **131**(5), 155. DOI: 10.1140/epjp/i2016-16155-x.

Caridi, F., Marguccio, S., Durante, G., Trozzo, R., Fullone, F., Belvedere, A., D'Agostino, M., and Belmusto, G. (2017b). "Natural radioactivity measurements and dosimetric evaluations in soil samples with a high content of NORM". *The European Physical Journal Plus* **132**(1), 56. DOI: 10.1140/epjp/i2017-11343-x.

Caridi, F., Messina, M., and D'Agostino, M. (2017c). "An investigation about natural radioactivity, hydrochemistry, and metal pollution in groundwater from Calabrian selected areas, southern Italy". *Environmental Earth Sciences* **76**, 668. DOI: 10.1007/s12665-017-7031-9.

Caridi, F., Acri, G., Belvedere, A., Crupi, V., D'agostino, M., Marguccio, S., Messina, M., Paladini, G., Venuti, V., and Majolino, D. (2021a). "Evaluation of the radiological and chemical risk for public health from flour sample investigation". *Applied Sciences* **11**(8), 3646. DOI: 10.3390/app11083646.

Caridi, F., Di Bella, M., Sabatino, G., Belmusto, G., Fede, M. R., Romano, D., Italiano, F., and Mottese, A. F. (2021b). "Assessment of Natural Radioactivity and Radiological Risks in River Sediments from Calabria (Southern Italy)". *Applied Sciences* **11**(4), 1729. DOI: 10.3390/app11041729.

Caridi, F., Messina, M., Belvedere, A., D'Agostino, M., Marguccio, S., Settineri, L., and Belmusto, G. (2019a). "Food Salt Characterization in Terms of Radioactivity and Metals Contamination". *Applied Sciences* **9**(14), 2882. DOI: 10.3390/app9142882.

Caridi, F., Paladini, G., Venuti, V., Crupi, V., Procopio, S., Belvedere, A., D'Agostino, M., Faggio, G., Grillo, R., Marguccio, S., Messina, G., and Majolino, D. (2021c). "Radioactivity, Metals Pollution and Mineralogy Assessment of a Beach Stretch from the Ionian Coast of Calabria (Southern Italy)". *International Journal of Environmental Research and Public Health* **18**(22), 12147. DOI: 10.3390/ijerph182212147.

Caridi, F., Santangelo, S., Faggio, G., Gnisci, A., Messina, G., and Belmusto, G. (2019b). "Compositional and Mineralogical Analysis of Marine Sediments from Calabrian Selected Areas, Southern Italy". *International Journal of Environmental Research* **13**(3), 571–580. DOI: 10.1007/s41742-019-00199-4.

Chopelas, A. (1999). "Estimates of mantle relevant Clapeyron slopes in the MgSiO3 system from high-pressure spectroscopic data". *American Mineralogist* **84**(3), 233–244. DOI: 10.2138/am-1999-0304.

Fiannacca, P., Cirrincione, R., Bonanno, F., and Carciotto, M. M. (2015). "Source-inherited compositional diversity in granite batholiths: The geochemical message of Late Paleozoic intrusive magmatism in central Calabria (southern Italy)". *Lithos* **236**, 123–140. DOI: 10.1016/j.lithos.2015.09.003.

Freeman, J. J., Wang, A., Kuebler, K. E., Jolliff, B. L., and Haskin, L. A. (2008). "Characterization of natural feldspars by raman spectroscopy for future planetary exploration". *Canadian Mineralogist* **46**(6), 1477–1500. DOI: 10.3749/canmin.46.6.1477.

Ghrefat, H. and Yusuf, N. (2006). "Assessing Mn, Fe, Cu, Zn, and Cd pollution in bottom sediments of Wadi Al-Arab Dam, Jordan". *Chemosphere* **65**(11), 2114–2121. DOI: 10.1016/j.chemosphere.2006.06.043.

Kolesov, B. A. and Geiger, C. A. (1998). "Raman spectra of silicate garnets". *Physics and Chemistry of Minerals* **25**(2), 142–151. DOI: 10.1007/s002690050097.

Kos, S., Dolenec, M., Lux, J., and Dolenec, S. (2020). "Raman Microspectroscopy of Garnets from S-Fibulae from the Archaeological Site Lajh (Slovenia)". *Minerals* **10**(4), 325. DOI: 10.3390/min10040325.

Krishnamurti, D. (1958). "The raman spectrum of quartz and its interpretation". *Proceedings of the Indian Academy of Sciences A* **47**, 276–291. URL: https://www.ias.ac.in/article/fulltext/seca/047/05/0276-0291.

Mckeown, D. A. (2005). "Raman spectroscopy and vibrational analyses of albite: From 25 °C through the melting temperature". *American Mineralogist* **90**(10), 1506–1517. DOI: doi:10.2138/am.2005.1726.

Mingsheng, P., Mao, H.-K., Dien, L., and Chao, E. C. T. (1994). "Raman spectroscopy of garnet-group minerals". *Chinese Journal of Geochemistry* **13**(2), 176–183. DOI: 10.1007/BF02838517.

Paiva, J. D. S., Farias, E. E. G., and Franca, E. J. D. (2015). "Assessment of the equilibrium of Th-228 and Ra-228 by gamma-ray spectrometry in mangrove soils". In: *INAC 2015: international nuclear atlantic conference Brazilian nuclear program State policy for a sustainable world*. Vol. 47. Brazil. URL: https://inis.iaea.org/search/search.aspx?orig_q=RN:47013750.

Papadopoulos, A., Christofides, G., Koroneos, A., and Stoulos, S. (2014). "Natural radioactivity distribution and gamma radiation exposure of beach sands from Sithonia Peninsula". *Open Geosciences* **6**(2), 229–242. DOI: doi:10.2478/s13533-012-0157-0.

Pirrotta, C., Barberi, G., Barreca, G., Brighenti, F., Carnemolla, F., De Guidi, G., Monaco, C., Pepe, F., and Scarfì, L. (2021). "Recent Activity and Kinematics of the Bounding Faults of the Catanzaro Trough (Central Calabria, Italy): New Morphotectonic, Geodetic and Seismological Data". *Geosciences* **11**(10), 405. DOI: 10.3390/geosciences11100405.

Qureshi, A. A., Tariq, S., Din, K. U., Manzoor, S., Calligaris, C., and Waheed, A. (2014). "Evaluation of excessive lifetime cancer risk due to natural radioactivity in the rivers sediments of Northern Pakistan". *Journal of Radiation Research and Applied Sciences* **7**(4), 438–447. DOI: https://doi.org/10.1016/j.jrras.2014.07.008.

Ramasamy, V., Meenakshisundaram, V., Venkatachalapathy, R., and Ponnusamy, V. (2011). "Influence of mineralogical and heavy metal composition on natural radionuclide concentrations in the river sediments". *Applied Radiation and Isotopes* **69**, 1466–1474. DOI: 10.1016/j.apradiso.2011.05.020.

Ravisankar, R., Chandrasekaran, A., Vijayagopal, P., Venkatraman, B., Senthilkumar, G., Eswaran, P., and Rajalakshmi, A. (2012). "Natural radioactivity in soil samples of Yelagiri Hills, Tamil Nadu,

India and the associated radiation hazards". *Radiation Physics and Chemistry* **81**(12), 1789–1795. DOI: 10.1016/j.radphyschem.2012.07.003.

Rosell, J. R., Ortega, X., and Dies, X. (1991). "Natural and artificial radionuclides on the northeast coast of Spain". *Health physics* **60**(5), 709–712. DOI: 10.1097/00004032-199105000-00010.

Rottura, A., Bargossi, G., Caironi, V., Delmoro, A., Maccarrone, E., Macera, P., Paglionico, A., Petrini, R., Piccarretta, G., and Poli, G. (1990). "Petrogenesis of contrasting Hercynian granitoids from the Calabrian Arc, Southern Italy". *Lithos* **24**, 97–119. DOI: 10.1016/0024-4937(90)90019-W.

"RUFF Library" (2021). URL: https://rruff.info/Spessartine/X050147.

Sabatino, G., Bella, M. D., Caridi, F., Italiano, F., Romano, D., Magazù, S., Gnisci, A., Faggio, G., Messina, G., Santangelo, S., Leonetti, F., and Tripodo, A. (2019). "Radiological assessment, mineralogy and geochemistry of the heavy-mineral placers from the Calabrian coast (South Italy)". *Journal of Instrumentation* **14**(05), P05015. DOI: 10.1088/1748-0221/14/05/P05015.

Shahrokhi, A. and Kovacs, T. (2021). "Radiological survey on radon entry path in an underground mine and implementation of an optimized mitigation system". *Environmental Sciences Europe* **33**(1), 66. DOI: 10.1186/s12302-021-00507-w.

Smyth, H. R., Morton, A., Richardson, N., and Scott, R. A. (2014). "Sediment provenance studies in hydrocarbon exploration and production: An introduction". *Geological Society Special Publication* **386**(1), 1–6. DOI: 10.1144/SP386.21.

Taskin, H., Karavus, M., Ay, P., Topuzoglu, A., Hidiroglu, S., and Karahan, G. (2009). "Radionuclide concentrations in soil and lifetime cancer risk due to gamma radioactivity in Kirklareli, Turkey". *Journal of environmental radioactivity* **100**(1), 49–53. DOI: 10.1016/j.jenvrad.2008.10.012.

United Nations Scientific Committee on the Effects of Atomic Radiation (UNSCEAR) (2000). *Sources and Effects of Ionizing Radiation: Report to the General Assembly, with Scientific Annexes*. New York: United Nations. URL: https://www.unscear.org/unscear/uploads/documents/publications/UNSCEAR_2000_Annex-A.pdf.

Vennari, C. E. and Williams, Q. (2021). "A high-pressure Raman study of FeTiO3 ilmenite: Fermi resonance as a manifestation of Fe-Ti charge transfer". *Physics and Chemistry of Minerals* **48**(9), 34. DOI: 10.1007/s00269-021-01151-9.

Vitale, S., Ciarcia, S., Fedele, L., and Tramparulo, F. D. (2019). "The Ligurian oceanic successions in southern Italy: The key to decrypting the first orogenic stages of the southern Apennines-Calabria chain system". *Tectonophysics* **750**, 243–261. DOI: 10.1016/j.tecto.2018.11.010.

Wang, A., Kuebler, K. E., Jolliff, B. L., and Haskin, L. A. (2004). "Raman spectroscopy of Fe-Ti-Cr-oxides, case study: Martian meteorite EETA79001". *American Mineralogist* **89**(5-6), 665–680. DOI: 10.2138/am-2004-5-601.

Warr, L. N. (2021). "IMA–CNMNC approved mineral symbols". *Mineralogical Magazine* **85**(3), 291–320. DOI: 10.1180/mgm.2021.43.

[a] Università degli Studi di Messina,
Dipartimento di Scienze Matematiche e Informatiche, Scienze Fisiche e Scienze della Terra,
Contrada Papardo, 98166 Messina, Italy

[b] Università della Calabria,
Dipartimento di Biologia, Ecologia e Scienze della Terra,
via Pietro Bucci, cubo 12B, piano 2, 87036 Arcavacata di Rende (CS), Italy

* To whom correspondence should be addressed | email: dmajolino@unime.it

Communicated 30 November 2021; manuscript received 9 March 2022; published online 7 December 2022